Mn(II) oxidation catalyzed by nanohematite surfaces and manganite/hausmannite core-shell nanowire formation by self-catalytic reaction

Sayako Inoué [a,b,c,*], Akira Yasuhara [d], Haruka Ai [d], Michael F. Hochella Jr [a,c,e], Mitsuhiro Murayama [a,e,f,*]

[a] *The Virginia Tech National Center for Earth and Environmental Nanotechnology Infrastructure (NanoEarth), 1991 Kraft Drive, Blacksburg, VA 24061, USA*
[b] *Center for the Environmental Implications of NanoTechnology (CEINT), Virginia Tech, Blacksburg, VA 24061, USA*
[c] *Department of Geosciences, Virginia Tech, Blacksburg, VA 24061, USA*
[d] *JEOL Ltd., 3-1-2 Musashino, Akishima, Tokyo 196-8558, Japan*
[e] *Energy and Environment Directorate, Pacific Northwest National Laboratory, Richland, WA 99354, USA*
[f] *Department of Material Science and Engineering, Virginia Tech, Blacksburg, VA 24061, USA*

Received 2 February 2019; accepted in revised form 7 May 2019; available online 24 May 2019

Abstract

The present study investigated the solid products of heterogeneous catalytic oxidation of aqueous Mn(II) by O_2 in the presence of hematite nanoparticles (NPs) using transmission electron microscopy (TEM), scanning TEM (STEM), and electron energy-loss spectroscopy (EELS). The oxidation experiments were conducted at room temperature (22 ± 2 °C) in solutions containing 10^{-3} M Mn(II) at pH 7.5 in the dark. During 48 h of reaction, a single-phase manganite (a Mn oxyhydroxide) nanowire was formed by way of metastable groutite and feitknechtite nanowires, both of which are polymorphs of manganite. Between 48 and 168 h, the manganite further altered to core-shell structured nanowires with hausmannite (a mixed valent Mn oxide) forming a very thin (2 nm) outer-shell on the manganite wire core. The formation of Mn-oxyhydroxide nanowires was catalyzed by the hematite NPs surface through electrochemical pathways. This is described via the electron transfer across a redox couple from adsorbed Mn(II) to another site with adsorbed O_2 via the band structure of the semiconducting hematite. On the other hand, the Ostwald step rule was operative in the sequential crystallization from metastable groutite and feitknechtite to stable manganite, which could have resulted from the differences in the surface free energies, sizes, and morphologies of product polymorphs at the nanoscale. The final product (at least in the time range of our experiments) exhibited manganite/hausmannite core-shell structures. This product is most likely to be formed by the reactions catalyzed by the manganite nanowires themselves. Microscopic investigation of interfacial changes in structure and chemistry at the nanoscale is key, and it can be essential to understand the kinetic and thermodynamic phenomena related to the redox chemistry and phase stability of nanoparticles in complex, heterogeneous systems such as natural environments.

Keywords: Manganite nanowire; Nanoparticle-catalyzed redox reaction; Core-shell structure; HRTEM; EELS

* Corresponding authors at: The Virginia Tech National Center for Earth and Environmental Nanotechnology Infrastructure (NanoEarth), 1991 Kraft Drive, Blacksburg, VA 24061, USA.
E-mail addresses: inouesayako@gmail.com (S. Inoué), murayama@vt.edu (M. Murayama).

https://doi.org/10.1016/j.gca.2019.05.011

1. INTRODUCTION

Manganese (Mn) is the 12th most abundant element in the Earth's crust (and therefore considered a minor element), but its (oxyhydr)oxides play a significant role in the geochemical cycling of elements in near-surface environments (e.g. Stumm and Morgan, 1996; O'Reilly and Hochella, 2003; Hochella et al., 2005a, b; Luther, 2016). Divalent Mn(II) is stable in solutions under relatively acidic and anoxic conditions without carbonate, sulfide, and phosphate ions, and therefore often mobile through soils and sediments. On the other hand, tri- and tetravalent Mn ions, Mn(III) and Mn(IV), are unstable as aqueous species and precipitate as (oxyhydr)oxides (called Mn oxides hereafter for simplicity) under oxic conditions. Oxidation of Mn(II) proceeds very slowly in homogeneous systems, if at all, with no help from biotic or abiotic catalysts (Diem and Stumm, 1984). Despite the importance of biotic Mn oxidation in many geologic systems (e.g. Tebo et al., 2004), nanomaterial surface-catalyzed Mn redox reaction also influences the precipitation and dissolution in soils and sediments (e.g. Madden and Hochella, 2005; Hochella et al., 2005a, b). As the oxidation of aqueous Mn (II) is catalyzed on the surfaces of nanomaterials in soils and sediments, Mn oxides precipitate to form particles and often films coating mineral grains and fracture surfaces in rocks. They often co-precipitate with other contaminant elements including arsenic, chromium, zinc, and copper (e.g. Hochella et al., 1999; O'Reilly and Hochella, 2003; Hochella et al., 2005a, b; Villalobos et al., 2005a, b; Grangeon et al., 2012). When the Mn oxides dissolve and/or transform to other solid phases, the co-precipitated contaminants will be released into the ambient solution. Thus, the redox reactions of Mn are closely linked to the geochemical cycling of the other elements in soils and sediments.

Fe (oxyhydr)oxide (Fe oxide hereafter) nanoparticles (NPs) are a common constituent of soils and sediments (Cornell and Schwertmann, 2003). They often coexist with Mn oxides (e.g. Jambor and Dutrizac, 1998, and references therein). Numerous laboratory studies have been performed to characterize the adsorption and oxidation behavior of Mn (II) on various Fe oxides (e.g. Sung and Morgan, 1981; Davies and Morgan, 1989; Junta and Hochella, 1994; Madden and Hochella, 2005; Wang et al., 2015; Lan et al., 2017). It has been shown that the presence of Fe oxide NP surfaces accelerates the oxidation of Mn(II) in solutions, and consequently the precipitation of Mn oxides. The rate of adsorption-oxidation of Mn was significantly greater on the surfaces of semiconducting materials such as hematite, goethite, and ferrihydrite than on those of insulating albite, amorphous $Al(OH)_3$, and montmorillonite (Junta and Hochella, 1994; Lan et al., 2017). The surface-catalyzed Mn(II) oxidation by Fe oxide NPs is linked to the semiconducting nature of Fe oxides, as described by the electron transfer (ET) process between Mn(II) and Fe oxide NPs (Madden and Hochella, 2005; Chernyshova et al., 2011a, b; Lan et al., 2017).

Different types of product Mn oxides can be obtained, depending on the experimental conditions such as temperature, pH, Mn concentration and the size of catalyst NPs (e.g. Bricker, 1965; Hem and Lind, 1983; Junta and Hochella, 1994; Wang et al., 2015; Lan et al., 2017). In addition, it is suggested that the product Mn oxide structure could be altered in response to continuous interactions with the surrounding aqueous Mn(II) ion bearing solution (e.g. Hem and Lind, 1983; Lefkowitz et al., 2013; Frierdich et al., 2016). Previous studies mainly focused on the macroscopic characterization of product Mn oxide structures and trend in describing the structural transformations. Comparatively little attention has been paid to the direct observation of each single particle. In the case where particle sizes are in the nanoscale, the surrounding environment has a greater impact on the structure of nanomaterials (Banfield and Zhang, 2001). This means that the final nanoscale Mn oxide products are influenced by the reactions between the catalyst NP and adsorbed Mn(II) ions as well as those between the (intermediate) product Mn oxides and surrounding solution. The distinction between two types of nanoscale particle-solution interactions has never been attempted in the previous studies. In the present study, the Mn oxidation experiments were conducted in air-saturated solutions containing hematite NPs at pH 7.5 and room temperature. The morphology, structure and chemical composition of individual particles of the product Mn oxide are characterized by transmission electron microscopy (TEM) and scanning TEM (STEM) along with electron energy loss spectroscopy (EELS). In this study, we elucidate the nanoscale interfacial reaction starting at nanohematite catalysts, and subsequently the reaction at the nanoscale Mn oxide product with a special emphasis on the ET process across the semiconducting NP.

2. METHODS

2.1. Synthesis of hematite NPs

All glassware was soaked in 5% (v/v) HNO_3 solution overnight followed by rinsing with the ultrapure water (18MΩ cm; MilliQ) prior to the experiments.

Hematite NP catalyst was synthesized by the forced hydrolysis of acidic ferric salt solution following the method 1 in Schwertmann et al., 2000. Briefly, a 2 L of 0.002 M HNO_3 solution in a glass Erlenmeyer flask was brought to 98 °C in an oven. Under vigorous stirring, a 16.16 g of $Fe(NO_3)_3{\cdot}9H_2O$ crystals (ACS reagent grade; ACROS Organics) was added to the solution to bring the ferric nitrate solution to an initial Fe concentration of 0.02 M. The solution was aged in the sealed Erlenmeyer flask for seven days at 98 °C. Then, the solution was cooled overnight and dialyzed using a dialysis membrane tube (size 27; Wako Pure chemical industries) to remove the residual salts for four days using the ultrapure water. The density of hematite NP suspension after the dialysis was 0.8 ± 0.05 g/mL, which leads to the estimated concentration of 15.2% (v/v). Synthesized hematite nanocrystals exhibited a rhombohedral shape with 30–40 nm in diameter (Fig. 1). Other Fe oxides such as ferrihydrite were not detected by TEM and X-ray diffraction (XRD) (Fig. 1).

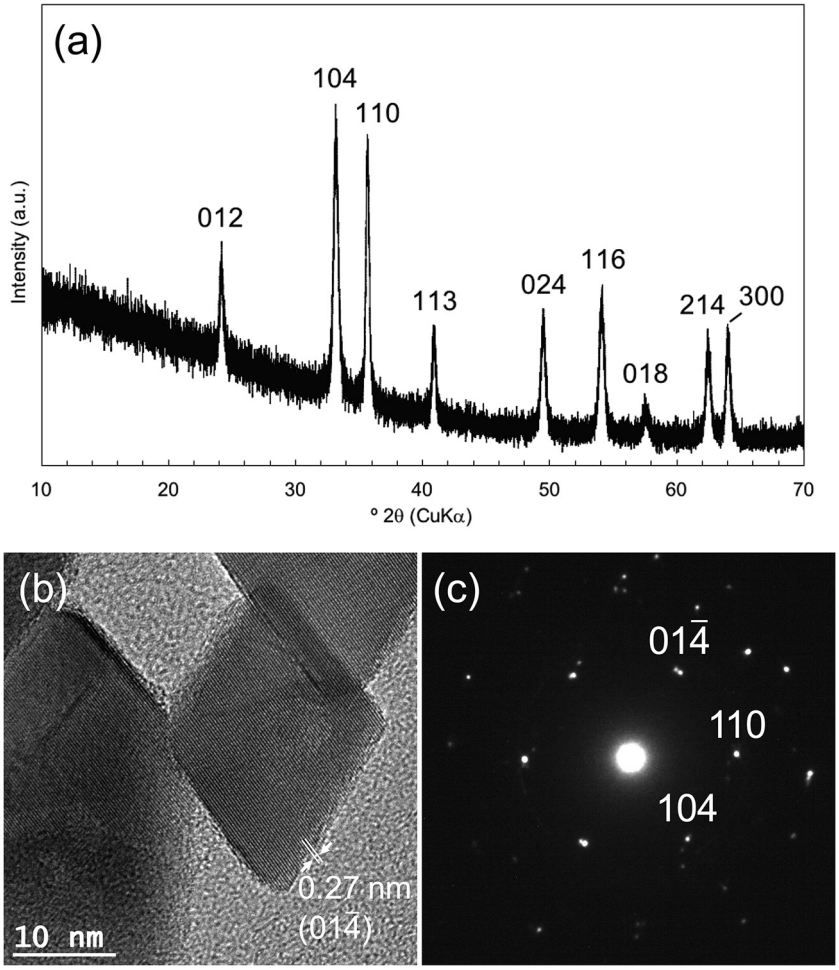

Fig. 1. (a) Powder XRD pattern of pre-reaction hematite NPs (b) HRTEM image of pre-reaction hematite NPs bounded by {1 0 4} family of planes (c) SAED pattern showing the hematite [44 1] orientation.

2.2. Mn oxidation experiments

A 20 mg of hematite NP suspension and 1 mL of 1 M PIPES buffer (piperazine-N, N′-bis (2ethanesulfonic acid); ≥99%; Sigma-Aldrich) were added to 50 mL of ultrapure water in a 50-mL polypropylene centrifuge tube. The PIPES buffer, a classic biochemical buffer, was used to keep pH at 7.5 and minimize the drift in pH. To the best of our knowledge, neither reduction nor oxidation of Mn oxides by the PIPES buffer has not been reported in the previous study. Hence, we assumed that the PIPES buffer has no or negligible influence to the experiments. A pH of 7.5 was chosen for this study because the solubility of hematite is lowest at this pH value (Baes and Mesmer, 1976). The concentration of PIPES buffer was 0.002 M, and the estimated concentration of hematite NP was 1.1×10^{-3}% (v/v). The pH of the suspension was adjusted to 7.5 by adding a 1 M NaOH and/or HCl solution. A 50 μL of 1 M $MnCl_2$ solution ($MnCl_2 \cdot 4H_2O$; ACS reagent grade; Sigma-Aldrich) was then added to the suspension under stirring. The initial Mn(II) concentration was 0.001 M. This Mn(II) concentration was chosen to depict the pathway of Mn oxide precipitation via metastable phases, and the interactions between $Mn(II)_{aq}$ and product Mn oxides over a wide range of Mn(II) concentration. The reaction mixture was continuously stirred either by magnetic stirrer or tumbler mixer for up to168 h (seven days). During the synthesis, the reaction mixtures were covered by aluminum foil or a Styrofoam box to minimize the photocatalytic effects. The drift in pH was monitored at regular intervals and adjusted to 7.5 by adding a few drops of 1 M NaOH and/or HCl solution if necessary. In most cases, the reaction mixtures experienced a noticeable pH drop to ~7.3 at the lapse of reaction time, 2 and 24 h, and hence a few μL of NaOH solution was added to bring pH back to 7.5 each time. It should be noted that the identical reaction products were obtained in the case where the drift in pH was negligible and neither NaOH nor HCl was added to the suspension. The experiments were conducted at room temperatures (22 ± 2 °C). The suspension was collected for the examination of solids at various time intervals: 2, 4, 8, 10, 12, 24, 36, 48, 120, and 168 h; each was dialyzed as soon as it was taken out. The dialysis took four days to complete. The same experimental runs were repeated three times to verify the reproducibility of results.

The variations in Mn(II) and Fe concentrations in solution were not monitored in the present study. The data were cited from Veeramani et al. (2013) who performed the hematite surface-catalyzed Mn oxidation under the same experimental conditions.

2.3. Characterization of product Mn oxides

The reaction products collected were examined by XRD, scanning electron microscopy (SEM), and TEM. Powder XRD was performed using a PANalytical Empyrean X-ray diffractometer in reflection geometry with a Cu K α ($\lambda = 1.54$ Å) X-ray source and Bragg-Bretano HD divergent beam optic. The incident beam path included a 0.02 rad Soller slit, 10 m beam mask, 1/2° fixed antiscatter slit, and 1/8° fixed divergence slit. A 0.02 rad Soller slit was used in the diffracted beam path. The suspension was dropped on low-background Si wafer sample holders and air-dried. The samples were rotated in place during the analysis. Diffraction intensities were collected from 10 to 70° 2θ in approximately 0.0036° increments per second using a GaliPIX^{3D} area detector system (PANalytical) operating in the line mode.

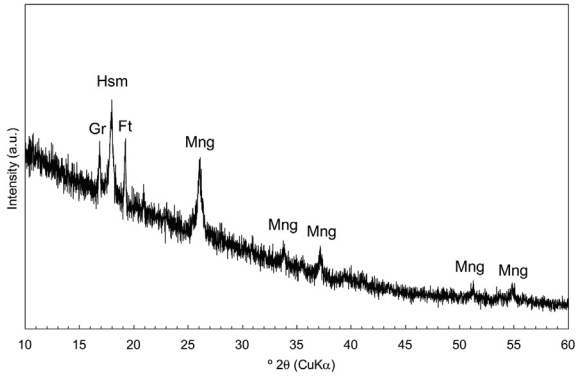

Fig. 2. Powder XRD pattern of synthesis product collected at 48 h after the reaction was initiated. Gr: groutite; Hsm: hausmannite; Ft: feitknechtite; Mng: manganite.

S/TEM samples were prepared by dropping an aliquot of the dialyzed suspension on copper TEM grids coated either by formvar or lacey carbon thin support film (Pacific Grid Tech, TedPella and EMS). Some of the prepared S/TEM grids were examined by a SEM (FEI Quanta 600 FEG) operated at 20 kV to survey macroscopic morphologies of solid phases. High resolution TEM (HRTEM) imaging and selected area electron diffraction (SAED) analyses were carried out by a JEOL JEM 2100 operated at 200 kV and a Thermo-Fisher (former FEI) Titan 80-300 operated at 300 kV. Energy dispersive X-ray spectroscopy (EDS) analysis was performed by a JEOL JEM 60-mm^2-window silicon drift detector based EDS system equipped on the JEM 2100. STEM analysis was done by the Titan 80-300. Electron energy-loss spectroscopy (EELS) and energy-filtered TEM (EFTEM) analyses were carried out on the Titan 80-300 equipped with a Gatan imaging filter (GIF-Tridiem 863) controlled by Gatan Digital Micrograph. EELS spectrum imaging was carried out by a Gatan imaging filter (GIF- Quantum ER) controlled by the Gatan Digital Micrograph equipped on a JEOL JEM F200 S/TEM operating at 200 kV. EELS spectrum images were collected at the camera length of 30 mm, GIF entrance aperture size of 5 mm, collection semi-angle (β) of 50 mrad, and energy resolution (full width at half maximum of zero-loss peak) of 0.2 eV.

The crystallographic calculations of the interface structure were done by the CrystalKit software (Total Resolution). Multi-slice image simulations were performed using the MacTempas software (Total resolution). The values for the spherical aberration and spread of defocus were set to 1.2 mm and 80 Å, respectively. The structure model for manganite was monoclinic $P2_1/c$, $a = 0.5304$ nm, $b = 0.5277$ nm, $c = 0.5304$ nm, $\alpha = \gamma = 90°$ and $\beta = 114.38°$ (Kohler et al. 1997) and that for hausmannite

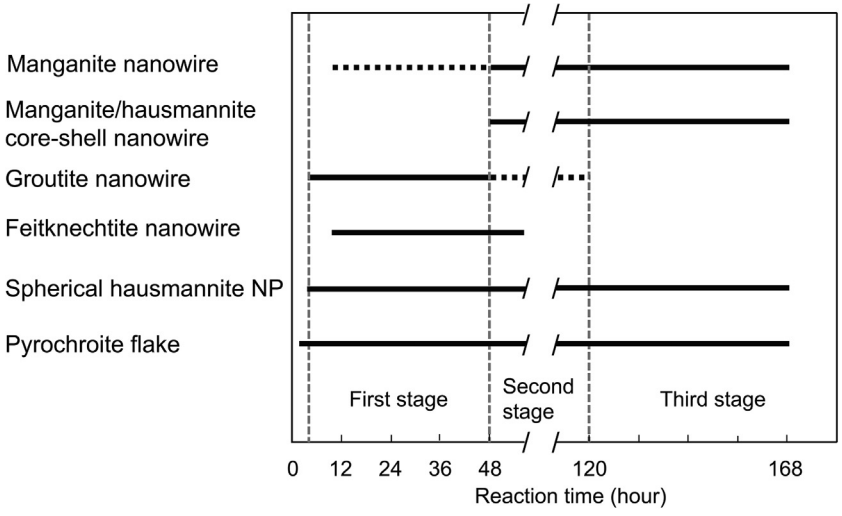

Fig. 3. Type of Mn oxides observed at different reaction times. First, second and third stages are marked in the figure. Thick dotted lines indicate that only one particle was observed by TEM in that period.

was tetragonal $I4_1/amd$, $a = b = 0.576$ nm, $c = 0.943$ nm, and $\alpha = \beta = \gamma = 90°$ (Aminoff, 1926).

3. RESULTS

3.1. Overview of reaction products

No solid Mn oxides were identified by XRD and TEM in the solutions collected during the first two hours of reaction. After four hours of reaction, six types of nanoscale Mn oxides were identified: wire-shaped groutite (α-MnOOH), feitknechtite (β-MnOOH) and manganite (γ-MnOOH), manganite nanowires with a hausmannite outer-shell (manganite/hausmannite core-shell nanowires), spherical hausmannite (Mn_3O_4) NPs, and pyrochroite ($Mn(OH)_2$) flakes (Figs. 2 and 3). The formation of Mn-carbonate minerals was not observed in the present study in contrast to some previous studies (e.g. Junta and Hochella, 1994; Chernyshova et al., 2011a, b). The product Mn oxides are summarized as a function of different sampling time in Fig. 3.

Mn oxide nanowires are the major products of this reaction. Groutite and feitknechtite nanowires were formed first, and then manganite nanowires were formed. Other

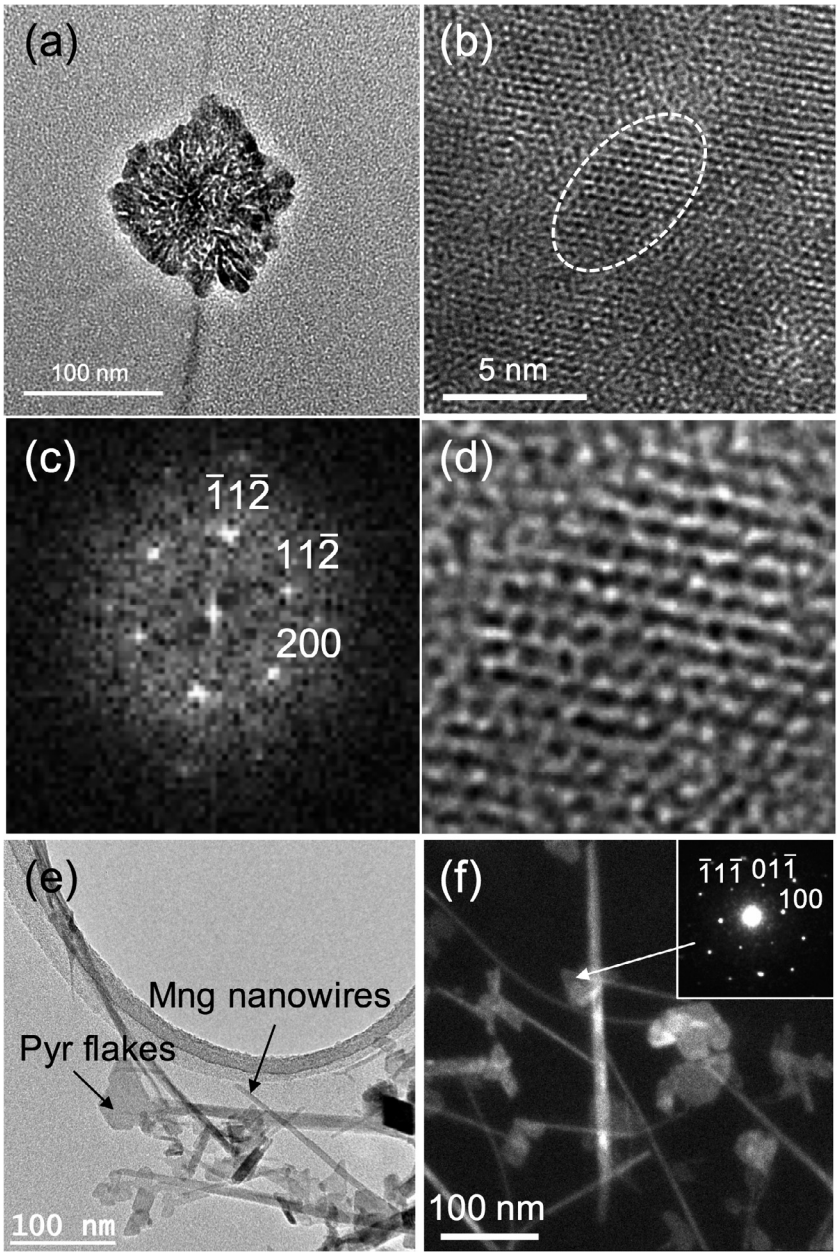

Fig. 4. TEM and STEM images of Mn oxide NPs. (a) Aggregates of spherical hausmannite NPs collected after 44 h of reaction. (b) HRTEM image of (a). A single hausmannite NP is highlighted. (c) FFT pattern from the vicinity of the highlighted NP in (b), corresponding to hausmannite [0 2 1]. (d) The IFFT image of c. (e, f) TEM image (e) and HAADF-STEM image (f) of flaky pyrochroite (Pyr) NPs and manganite (Mng) nanowires. The inset in (f) shows the ED pattern of a pyrochroite NP along [0 1 1].

than these products, small amounts of spherical hausmannite NPs and flaky pyrochroite were always identified in the samples regardless of the sampling time (Figs. 3 and 4). The spherical hausmannite NPs usually aggregated to form a 50–80 nm cluster (Fig. 4a). The SAED and fast Fourier transform (FFT) patterns obtained from the aggregate indicated that each particle of hausmannite is a single crystal (Fig. 4b–d). The hausmannite NPs did not change in size over the course of reaction. The sizes of single-crystal pyrochroite flakes (Fig. 4e and f) were also constant throughout the reaction. In contrast, the Mn oxide nanowires increased in size over 168 h of reaction (Fig. 5). The Mn oxide products were seldom in contact with hematite NPs. EDS analyses showed that the nanoscale Mn oxides contained no trace of Fe. The spherical hausmannite aggregates mentioned above should be distinguished from the hausmannite outer-shell which formed on the surfaces of manganite nanowire at the latest stage of reaction (discussed below).

3.2. Evolution of product Mn oxide nanowires

Based on the different structures of product Mn oxide nanowires, the entire reaction can be divided into three stages (Fig. 3), i.e., the first (4–48 h), second (48–120 h), and third stages (120–168 h). SAED analyses revealed that both groutite and feitknechtite nanowires were the characteristic of the first stage of reaction (Fig. 6). The sizes of nanowires ranged from 20–200 nm in length and 2–7 nm in diameter as measured by TEM (Fig. 5). Groutite and feitknechtite are known as metastable polymorphs of MnOOH (Bricker, 1965; Fritsch et al., 1997). The structure of groutite is composed of the edge-sharing double chains of MnO_6 octahedra which result in the 1×2 tunnel structure along <0 0 1> (Kohler et al., 1997). In comparison with the known structure of groutite, the long axis of product groutite nanowires was parallel to the <1 0 0> direction along the tunnel (Fig. 5a and b). Feitknechtite is considered to have a layer structure which is isotypic with pyrochroite (Bricker, 1965). Identification of feitknechtite nanowires was done by comparing the d-spacing measured on a ring SAED pattern (Fig. 5d) and the peak positions in powder XRD patterns (Fig. 2) with the data reported by Bricker (1965).

At the second stage of reaction, the single-phase manganite nanowires became the major product instead of groutite and feitknechtite (Figs. 3 and 7). Groutite and feitknechtite associated with manganite were scarcely observed by TEM. Manganite is the most stable MnOOH polymorph (Bricker, 1965; Post, 1999). It has a deformed rutile structure composed of the single MnO_6 octahedral chains showing a 1×1 tunnel structure along <1 0 1> (Kohler et al., 1997). The product manganite nanowires exhibited 200 –1000 nm in length and 10–20 nm in diameter (Fig. 6). The length of nanowires varied among repeated experimental runs, whereas the diameter was almost constant. The continuous lattice fringes along the long axis of manganite nanowires corresponded to a set of $(1\,1\,\bar{1})$ planes (Fig. 7c). It is known that the long axis of manganite is parallel to the <1 0 1> (Kohler et al., 1997), and thus the product manganite nanowires were elongated along the tunnel (Fig. 7a and d).

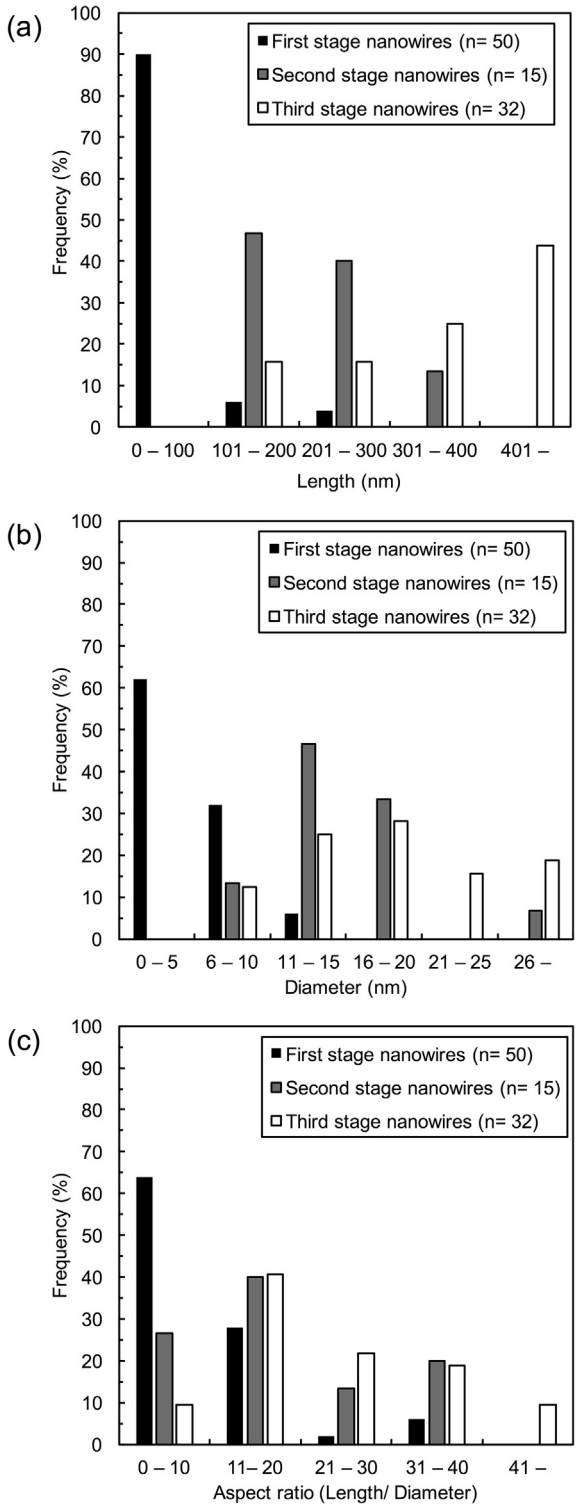

Fig. 5. The distributions of length (a), diameter (b) and aspect ratio (length/diameter) (c) of first, second and third stage nanowires. The length and diameter were measured on the TEM images of samples collected from the same experimental run. n: number of nanowires examined.

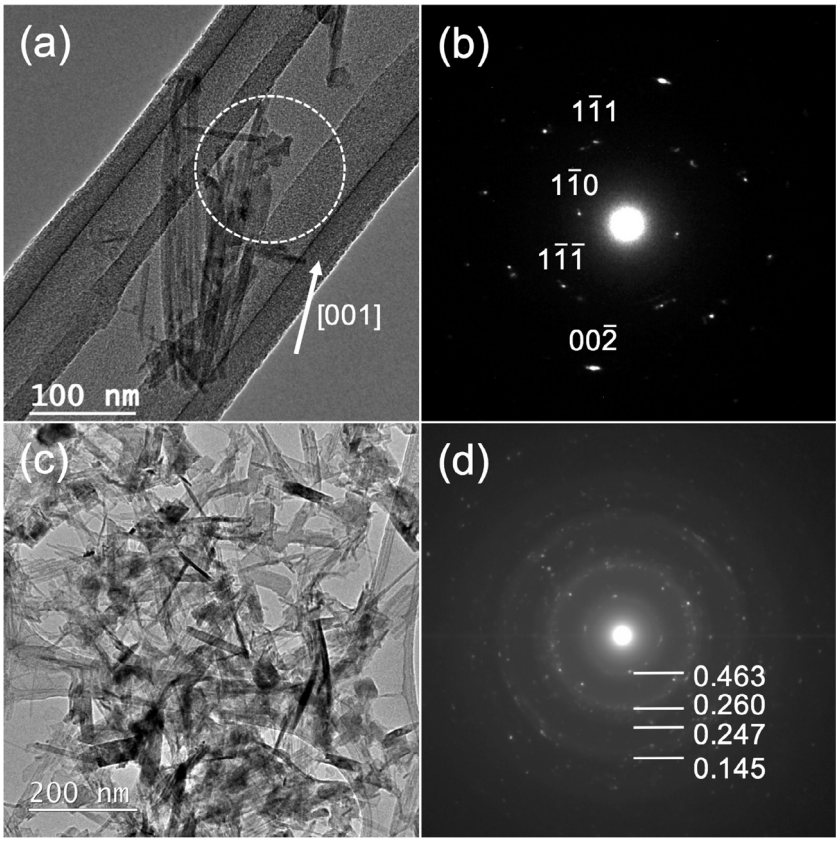

Fig. 6. (a) Bright field (BF) images of 36-h groutite nanowires. The groutite [001] is indicated by the arrow. (b) A SAED pattern of the highlighted area in (a), showing groutite [1 1 0]. (c) 24-h feitknechtite nanowires. (d) A ring SAED pattern of (c). The d-spacings of rings in nm are shown, which corresponds to the feitknechtite reported by Bricker (1965).

The major product at the third stage exhibited the manganite/hausmannite core-shell structure (Fig. 3). The entire surface of the manganite nanowires, including the wire tips, was covered by a 2–3 nm thick outer-shell (Figs. 8 and 9). The core-shell nanowires could not be distinguished from the single-phase manganite nanowires only by their morphology (Figs. 7 and 8), but it was possible to determine the nature of the core/shell structure by very careful HRTEM and EELS examinations. In addition, the outer-shell could be identified as a Mn oxide by EDS analyses. The FFT pattern obtained from the core part of manganite/hausmannite nanowire displayed the [1 2 $\bar{1}$] zone axis with the long axis parallel to [1 0 1] and the (1 1 $\bar{1}$) lattice fringes (Figs. 8 and 9). The (1 1 $\bar{1}$) lattice fringes with a spacing of 0.34 nm run along the sidewall of manganite nanowires (Fig. 8b). The FFT pattern from the outer-shell exhibited the lattice fringes of 0.29 nm almost perpendicular to the side wall of the nanowire (Fig. 8b). The FFT pattern was obtained from the vicinity of the interface between outer-shell and core-nanowire (Fig. 8c). Fig. 8d shows the interface in the inverse FFT (IFFT) image of Fig. 8c. To highlight the interface, the diffraction spots related to the outer-shell structure (marked in Fig. 8c) are excluded using a twin-oval masking tool on the Digital Micrograph software (Fig. 8d). The IFFT image generated from the Fig. 8d revealed that the 0.34 nm lattice fringes were not continued in the outer-shell (Fig. 8e). The FFT patterns from the outer-shell and core-nanowire in the different core-shell nanowire are compared (Fig. 9). In the outer-shell FFT pattern, there are diffraction spots which are not seen in that of core-nanowire (Fig. 9a). These spots cannot be explained by the manganite structure, but can be explained by the hausmannite structure, specifically [01 $\bar{2}$]. It should be noted that the core-shell structure was only observed in the manganite nanowires collected after 48 h.

3.3. Determination of Mn oxidation states

As mentioned above, the HRTEM analyses suggested that the third stage product is manganite/hausmannite core-shell nanowires. The average Mn oxidation states were determined by EELS spectrum imaging which acquired a series of EELS spectra from regions of 100 pixels × 50 pixels across the sample with a pixel resolution of 1 nm/pixel. An annular dark field (ADF)-STEM image of the corresponding area showed that there were two types of nanowires in the field of view (Fig. 10a). Core-loss EELS spectra were extracted from a 2 nm × 22 nm area in the respective core-nanowire (box 4) and outer-shell (box 1) of a 168-h nanowire marked in the Fig. 10a. In Fig. 11a,

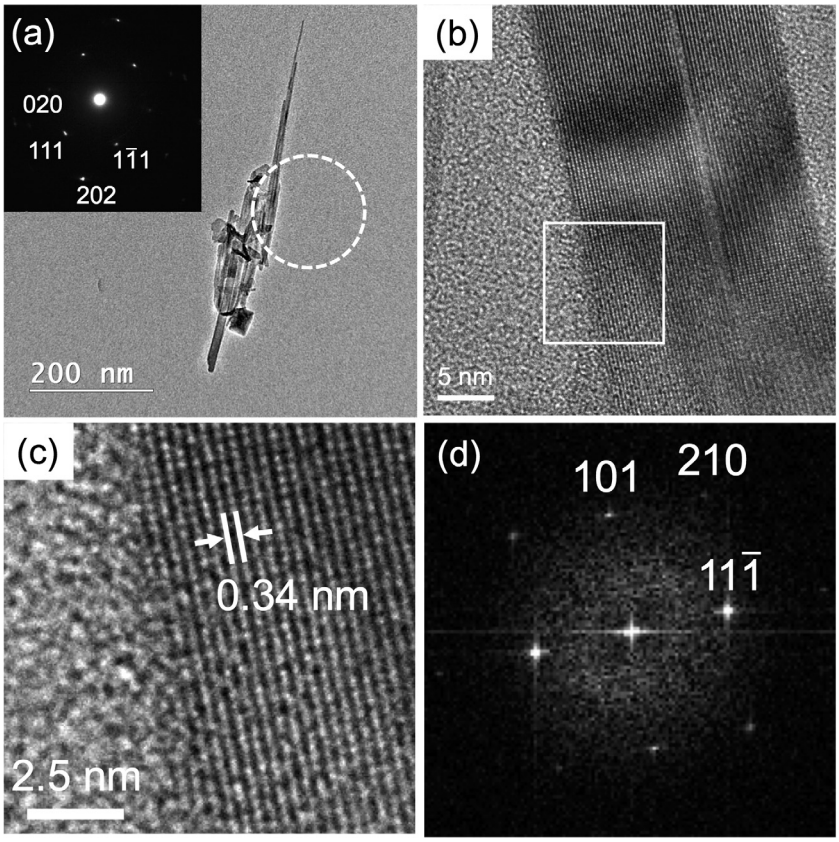

Fig. 7. (a) TEM image of 48-h nanowires and its SAED pattern (inset). The SAED pattern was obtained from the area indicated by the dotted circle and corresponds to manganite [2 0 $\bar{2}$]. (b) HRTEM image of single-phase manganite nanowire. (c) The magnified image of area in b indicated by the solid square exhibiting the lattice fringes which correspond to a set of manganite (1 1 $\bar{1}$) planes (0.34 nm). (d) FFT pattern of the square area in (b) showing manganite [$\bar{1}$ 2 1].

two peaks (p1 and p2) located between 530 and 550 eV correspond to the O-*K* absorption edge, which represents the transition from oxygen 1 $s_{1/2}$ state to molecular orbitals with oxygen 2p character (Kurata and Colliex, 1993). The Mn-L_2 and -L_3 edges appeared between 640 and 660 eV (Fig. 11b). They represent the electronic transitions from Mn $2p_{1/2}$ and $2p_{2/3}$ states to molecular orbitals with 3d character (Kurata and Colliex, 1993). The separation between two O-*K* peaks, the chemical shift of Mn-$L_{2,3}$ peaks, and the Mn L_2 to L_3 white-line intensity ratio (I(L_3)/I(L_2)) are known to reflect the average Mn oxidation state in Mn oxide compounds (Rask et al., 1987; Paterson and Krivanek, 1990; Kurata and Colliex, 1993; Tan et al., 2012). The O-*K* and Mn-$L_{2,3}$ edges shape in the core-nanowire spectrum was in good agreement with the manganite spectra reported in the previous studies (Rask et al., 1987; Tan et al., 2012). Compared to the core-nanowire spectrum, the decrease in the O-*K* peaks separation, increase in the I(L_3)/I(L_2) ratio, and chemical shift of Mn-$L_{2,3}$ peaks toward the lower energy side were visible in the outer-shell spectrum (Fig. 12). The characteristics indicate that the outer-shell has lower average Mn oxidation state than the core-nanowire; thereby it is most likely hausmannite (Tan et al., 2012).

The spatial distribution of Mn oxidation states was mapped using the multiple linear least squares fitting method (MLLS) (Leapman and Swyt, 1988). MLLS can be used to fit a number of reference spectra and/or model to a dataset (Maigné and Twesten, 2009). The MLLS routine fits reference spectra to a dataset and tells how much of each reference spectrum is present. When applied to spectrum imaging, this method can provide not only the relative contribution of the reference spectra but also the distribution of them. The Mn-$L_{2,3}$ edges shown in Fig. 11b were used as the reference spectra for Mn(II, III) (Fig. 10b) and Mn(III) (Fig. 10c) in the present study. The Mn(II, III)-bearing phase, i.e. hausmannite, was localized at the periphery of nanowires (Figs. 10b and 12c). The thickness was about 3 nm, which was consistent with the thickness of the outer-shell measured on the HRTEM images (Fig. 9). These results strongly support that the outer-shell has the hausmannite structure.

In summary, the MnOOH nanowires produced in the present experiments experienced structural conversion from metastable groutite and feitknechtite to stable manganite in the first 48 h of reaction. The single-phase manganite subsequently altered to manganite/hausmannite core-shell nanowire.

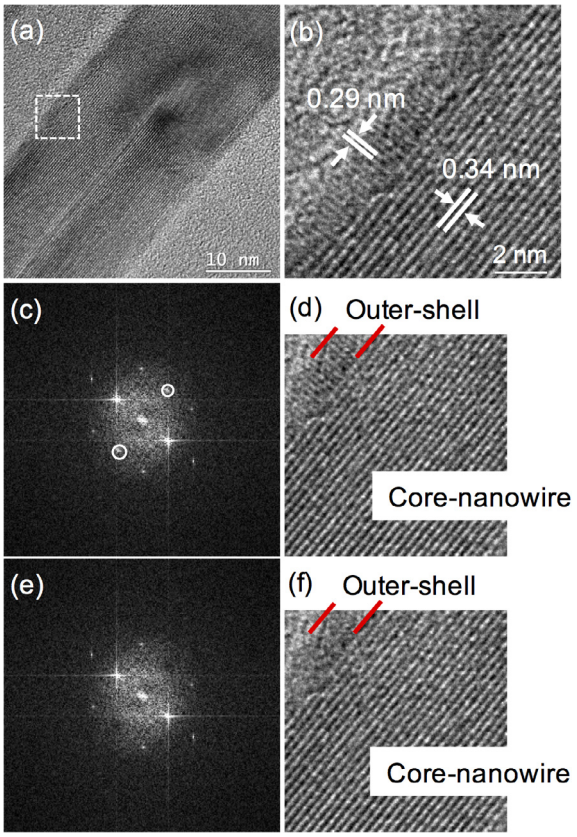

Fig. 8. (a) HRTEM image of 168-h manganite/hausmannite core-shell nanowires. (b) Magnified image of area indicated by the dotted square in (a). The lattice fringes run along the long axis of the nanowire (0.34 nm) and also perpendicular to the sidewall of the nanowire (0.29 nm). (c) FFT pattern from the core-shell nanowire. The spots associated with the 0.29 nm lattice fringes are highlighted. (d) IFFT image of (c). The interface between outer-shell and core-nanowire is indicated. (e) FFT pattern after the spots highlighted in (c) are excluded by twin-oval mask. (f) IFFT image of (e). It is clear that the 0.34 nm lattice fringes are not present in the outer-shell.

3.4. Relationships between hematite NP catalysts and MnOOH nanowires

The hematite NPs used as a catalyst have a rhombohedral morphology bounded by either the {1 1 0} or {1 0 4} facets with particle sizes of 30–40 nm (Fig. 1b and c). No significant changes in the morphology and crystal structure of hematite NPs were recognized throughout the reaction. No crystalline Mn oxide phase was identified by SAED of the post-reaction hematite NPs. Neither dissolution of Fe was observed in solution (Veeramani et al., 2013). The only change observed on the post-reaction hematite NPs was that they were covered by a thin layer of solid mater which is brightly imaged in the TEM images (Fig. 13). The presence of Mn on hematite NP aggregates was confirmed by EDS analyses regardless of the sample collection time. When the distribution of Mn in the hematite NP aggregates was more closely examined by EFTEM elemental mapping (Ahn, 2004; Egerton, 2011), the Fe (Fe-$L_{2,3}$ edge) map highlighted the sharp rhombohedral outline of hematite NPs, whereas the outline of aggregate highlighted on Mn (Mn-$L_{2,3}$ edge) and O (O-K edge) maps was somehow blur and in agreement with that of the brightly imaged outer layer in TEM image (Fig. 13). Measuring the diameters of two NPs which appeared not to be overlapped with others (for example, marked NP1 and 2 in Fig. 13), the diameters measured on the Mn and O maps were larger than those on the Fe map (Table 1). The diameter on the Mn and O maps was coincident with those including the brighter contrast outer layer. The diameter on the Fe map matched with the size of darker contrast NPs. This trend and brightly imaged outer layer in the TEM image were observed in other post-reaction hematite NP aggregates as well.

The supplementary experiments of Mn oxidation in the absence of hematite NPs was conducted in the dark. No MnOOH nanowire was formed in the absence of hematite NP. However, when small amounts of NaOH were added to the solutions, pyrochroite flakes were formed. This was consistent with previous experimental results (Veeramani et al., 2013) in which no formation of Mn oxide nanowires was recognized in the solutions without having catalyst hematite NPs, as well as no change in the Mn concentration in solution during the elapsed reaction time.

4. DISCUSSION

4.1. Role of hematite NPs as catalysts in the Mn oxidation

The EFTEM elemental imaging exhibited the presence of Mn on the post-reaction hematite NPs (Fig. 13), indicating that adsorption-oxidation of Mn occurred on the surfaces of hematite NPs during reaction. Mn(II) oxidation catalyzed by the hematite NP surfaces has been described as the ET process between Mn(II) and O_2 adsorbed on the surfaces (e.g. Junta and Hochella, 1994; Madden and Hochella, 2005; Chernyshova et al., 2011a,b; Lan et al., 2017). Different mechanisms for the ET process have also been proposed. Chernyshova et al. (2011a,b) proposed that the hematite surface-catalyzed Mn(II) oxidation in the dark can be described as the ET process at the semiconductor-electrolyte interface. Hematite is an n-type semiconductor with electrons as carriers (Gardner et al., 1963; Chernyshova et al., 2010; Wang et al., 2011). In the n-type semiconductor, the Fermi level (E_F) lies just below the conduction band edge energy (E_{CB}) (Fig. 14a). Because the ET across the semiconductor-electrolyte interface occurs through a narrow distribution of energies near the bottom of the conduction band edge at the interface E_{CB}, the distributions of filled or empty energy levels of redox couples should match the positions of the conduction band at the interfaces (Morrison, 1990).

The electrochemical energetics in the present system are schematically illustrated in Fig. 14. The band gap energy (E_g) of hematite NPs (particle sizes of 30–40 nm) used in this study was assumed to be 2.55 eV at pH 7.5 from the Tauc-Mott plot in Chernyshova et al. (2010) who determined E_g of hematite NPs with a diameter of 38 nm. In addition, assuming that the electronic properties of present hematite NPs are similar to those of a polycrystalline hema-

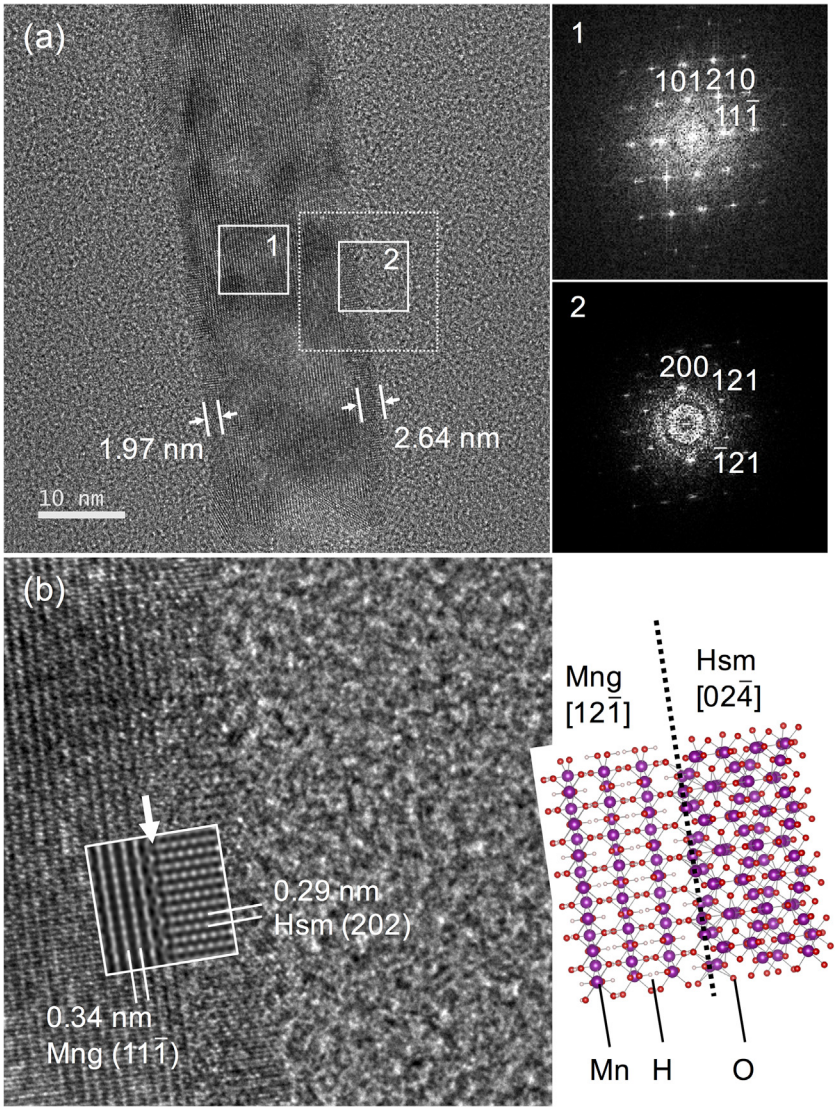

Fig. 9. (a) HRTEM image of 168-h manganite/hausmannite core-shell nanowire. The thickness of the outer-shell layers is shown. The FFT patterns are from the manganite core-nanowire showing [1 2 $\bar{1}$] (labeled 1) and hausmannite outer-shell showing [0 2 4] (labeled 2). (b) Magnified image of the manganite/hausmannite interface indicated by a dotted square in (a). The schematic diagram is the simulated HRTEM image of the interface showing the atomic structure of the proposed interface shown in (b), drawn using VESTA software (Momma and Izumi, 2011).

tite electrode (Chernyshova et al., 2011a), the flat band potential (U_{fb}) and the energy gap between E_F and the bottom of the conduction band are −0.019 V on the standard hydrogen electrode scale (SHE) and 0.29 eV at pH 7.5, respectively (Kennedy and Frese, 1978). The absolute energy of SHE is −4.44 eV, and the absolute vacuum scale (eV) is related to the conventional electrochemical potential Eh (V) by the relation: E(eV) = Eh(V vs SHE) + 4.44 (Morrison 1990). The U_{fb} corresponds to the position of E_F of semiconductor at the flat band condition, which equals the intrinsic E_F of semiconductor. The E_{CB} at flat band condition is −0.31 V (vs SHE).

Here, the overall Mn(II) oxidation is represented by reaction (1)

$$Mn^{2+}_{aq} + \tfrac{1}{4}O_{2aq} + \tfrac{3}{2}H_2O \rightarrow MnOOH_c + 2H^+. \quad (1)$$

The reaction (1) can be split into two half-reactions of oxidation (2) and reduction (3):

$$Mn^{2+}_{aq} + 2H_2O \rightarrow MnOOH_c + 3H^+ + e^- \quad (2)$$

and

$$O_{2aq} + 4H^+ + 4e^- \rightarrow 2H_2O \quad (3)$$

where subscripts *aq* and *c* stand for the aqueous and crystalline phases, respectively. The redox potential of O_2/H_2O redox couple (reaction (3)) at pH 7.5 is 0.77 V (vs SHE). It is also calculated from the Nernst equation that the redox potentials of the redox couple γ-MnOOH (man-

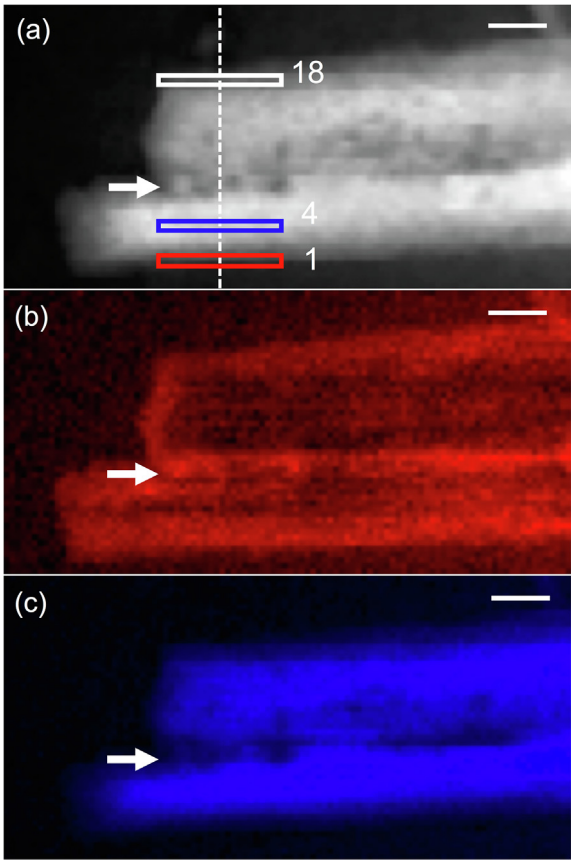

Fig. 10. (a) ADF-STEM image of the area where the spectrum images were obtained and shown in (b) and (c). (b, c) Results of MLLS fitting using the outer-shell (b) and core-nanowire (c) spectra. Mn-$L_{2,3}$ edges obtained from box 4 and 1 indicated in (a) are used for the MLLS fitting of (b) and (c), respectively. The arrows indicate the boundary between two nanowires. The contrast profiles of b and c are extracted from a line shown in a. The scale bars in the upper right of the images are 10 nm. Box 18 is referred to in Fig. 12.

ganite)/Mn^{2+} are 0.29 V (vs SHE) at pH 7.5, using the thermodynamic data in Bard et al. (1985). Taking the uncertainty in the thermodynamic parameters of fine-grained metastable phase (Navrotsky, 2001) into account, only manganite/Mn^{2+} redox potential will be considered below.

In the presence of dissolved O_2 in electrolyte, the oxygen is preferably adsorbed on the most negatively charged facets on hematite, and can further be reduced (McAlpine and Fredlein, 1983). In Fig. 14a, the relative positions of the E_{CB} and the redox potential of the half-reaction (3) allow the adsorbed O_2 to be reduced by capturing free electrons in hematite (Chernyshova et al., 2011a, b). Such interfacial ET generates a space charge layer in the semiconductor, and results in the conduction and valence band bending (Fig. 14b). Electrons flow from semiconductor hematite to the adsorbed oxygen until the equilibrium is attained between semiconductor and redox couple (3) at which the E_F of the semiconductor is equal to the redox potential of O_2 reduction. The resulting downward shift of E_F makes the ET from Mn(II) to hematite possible (Fig. 14b). The ET can be caused by the surface states-mediated catalytic reaction by the electrons tunneling across the interfacial barrier under strongly electron-depleted conditions (Morrison, 1990; Chernyshova et al., 2011a, b). When electrons are injected into the semiconductor, these electrons are moved away from the Mn(II) adsorbed on the anodic surface sites by the potential drop in the space charge layer toward the O_2 adsorbed cathodic surface sites where oxygen consumes the electrons (Fig. 14b). Thus, the net reaction (1) can proceed via the electrochemical route which is promoted by n-type semiconductor hematite.

Another proposed ET mechanism involves the inner-sphere adsorption of Mn(II) on the Fe oxide surfaces which promotes the oxidation of Mn(II) by reducing the activation energy for ET which results in the ET between complexed Mn(II) and O_2 (Davies and Morgan, 1989; Stumm and Morgan, 1996). For the semiconducting NPs, the ET process is achieved by the direct injection of electrons between Mn(II)aq and the conduction band of semiconducting NPs (Schoonen and Strongin, 2005). Such an interfacial catalytic pathway considers that the reduction and oxidation half-reactions occur at the same adsorption site or neighboring adsorption sites. In this study, the manganite/Mn^{2+} redox potential (reaction (2)) is below the E_{CB}, suggesting that the direct electron injection into the conduction band of the semiconductor is unlikely to happen (Xu and Schoonen, 2000). In order to clarify the mechanism of the ET process, further consideration on the electrochemical properties of catalyst NPs and product Mn oxides will be necessary.

4.2. Role of hematite NPs in the formation MnOOH structures

When the redox potentials of the manganite/Mn^{2+} with those of α-MnOOH (groutite)/Mn^{2+} (0.35 V (vs SHE)) and β-MnOOH (feitknechtite)/Mn^{2+} (0.49 V (vs SHE)) are compared, the latter two are positioned below the redox potential of manganite/Mn^{2+} redox potential, indicating that the formation of manganite may be easier to achieve. This electrochemical consideration apparently contradicts the present experimental results in which groutite and feitknechtite formed first, not manganite. It is suggested that the incipient formation of metastable groutite and feitknechtite may be controlled by different mechanisms from the hematite-catalyzed Mn(II) oxidation. The possible mechanism of metastable groutite and feitknechtite formation will be discussed in the next section. According to the previous studies in the absence of hematite (Stumm and Giovanoli, 1976; Hem and Lind, 1983; Murray et al., 1985; Kirillov et al., 2009), hausmannite precipitated first and subsequently altered to manganite with aging when Mn(II) in solutions with similar Mn(II) concentration and pH to the present study was oxidized in the presence of O_2 at room temperature. On the other hand, the precipitation of feitknechtite and groutite was observed when the experiments were conducted under similar chemical conditions but at different temperature (near 0 °C) (Hem and Lind, 1983). In this study, the hausmannite NP aggregates

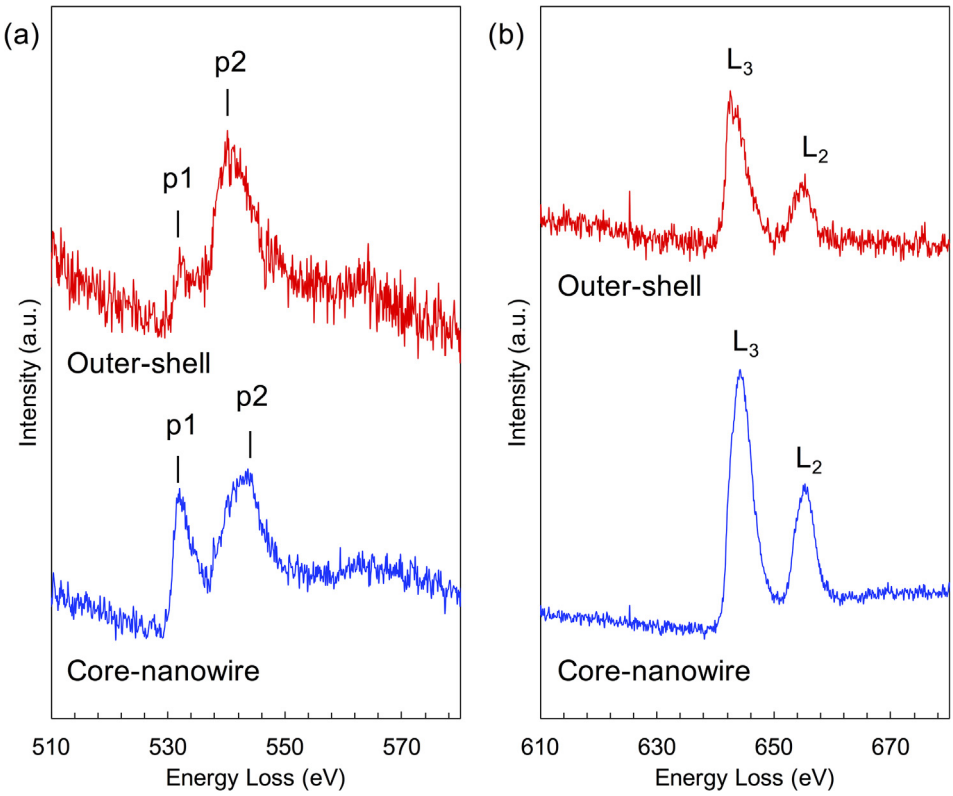

Fig. 11. Core-loss EELS spectra of the O-K edge (a) and Mn-$L_{2,3}$ edge (b) extracted from the outer-shell and core-nanowire. The outer-shell and core-nanowire spectra were extracted from boxes 1 and 4 in Fig. 10(a), respectively. The O-K edge onset energy in (a) is 529.6 eV for outer-shell and 529.3 eV for core-nanowire. The Mn-L_3 onset energy and $I(L_3)/I(L_2)$ ratio in (b) is 639.3 eV and 2.8 for outer-shell, and 639.7 eV and 2.3 for core-nanowire.

did not change in size, shape and structure during the reaction, suggesting that they are not the precursor of manganite nanowires. Rather, TEM results indicated that the feitknechtite and groutite appear to be a precursor of manganite nanowire. This conclusion is consistent with the results of Mn(II) oxidation on the surfaces of hematite by Junta and Hochella (1994). In their case, the feitknechtite was directly precipitated and no hausmannite formation was observed. Comparing the results in the previous studies without hematite with those in this study and Junta and Hochella (1994), it is concluded that the hausmannite formation at intermediate stages is skipped by the presence of hematite NPs.

In the present study, no crystalline Mn oxide phase was found on the surfaces of hematite NPs after reaction even with the use of tumbler mixers which was able to supply gentle stirring to reaction mixtures. On the other hand, Junta and Hochella (1994) observed the precipitation of a feitknechtite layer on cleaved hematite surfaces. It remains unsolved whether such difference in modes of occurrence of the products is due to the influence of the size of hematite catalyst or the stirring. However, the adsorption of Mn on the surfaces of hematite NPs revealed by EDS analyses and EFTEM mapping suggested that the hematite NPs not only catalyze Mn(II) oxidation, but also provide a site for at least initial nanowire formation.

4.3. First stage formation of groutite/feitknechtite and their transformation to manganite

TEM observations indicated that the groutite and feitknechtite nanowires are formed by way of manganite nanowire formation. The thermodynamic equilibria for the three MnOOH polymorphs are illustrated in Fig. 15a using reaction (1). The differences in the solubility of solid phases predict that when the oxidation of Mn(II) proceeds in the solution with 10^{-3} M Mn and pH 7.5, the MnOOH would precipitate in the order of feitknechtite, groutite, and manganite with Mn(II) concentration decrease. This thermodynamic prediction is nearly concordant with the present observations. Such sequential crystallization of polymorphs may be explained by the Ostwald Step Rule. Whether or not the Ostwald Step Rule is operative in the system is ascribed to the differences in the nucleation rates of thermodynamically stable and metastable phases (Markov, 1995). The differences in nucleation rates among different polymorphs are related to the surface free energies and their morphologies at the given reaction conditions. In general, the metastable phases have smaller surface free energies than stable phases, which leads to crossovers in the stability of polymorphs at the nanoscale (Navrotsky et al., 2010; Navrotsky, 2011). Feitknechtite has a layer structure (Bricker, 1965), while groutite and manganite have tunnel

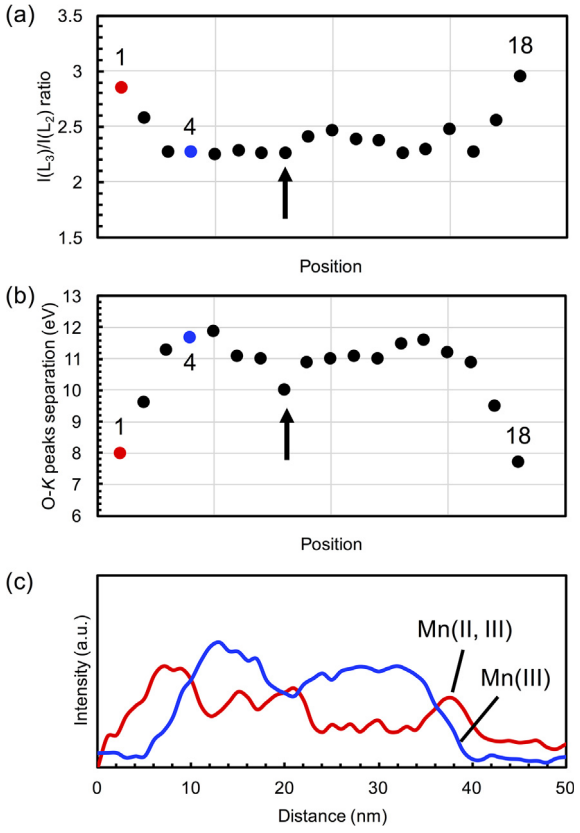

Fig. 12. The cross-sectional profiles of $I(L_3)/I(L_2)$ ratio (a) and O-K peaks separation (b). The numbers (1, 4 and 18) indicate the positions of boxes in Fig. 10(a). Arrows indicate the interface between two nanowires shown in Fig. 10. (c) The contrast profiles of the phase maps in Fig. 10(b) (Mn(II,III)) and (c) (Mn(III)). The horizontal axis shows the distance from the bottom of the maps.

structures (Kohler et al, 1997). From the structural points of view, topotactic transformation from a layered structure to a tunnel structure may be possible as seen in the vernadite-to-todorokite transformation (Bodeï et al., 2007). On the other hand, the structural conversion from groutite (1×2 tunnel) to manganite (1×1 tunnel) requires the reconstruction of MnO_6 octahedra associated with dissolution and recrystallization processes. Because the direct contact between the MnOOH nanowire and hematite NPs have not been observed in this study, how the ET on hematite surfaces influence the crystallization and dissolution-recrystallization processes are unclear. It is necessary to quantitatively understand not only the kinetics of Mn oxidation related to the ET on hematite catalysts, but also the thermodynamics of product polymorphs with different sizes and morphologies at the nanoscale.

4.4. Formation of hausmannite outer-shell on manganite core

The third stage of reaction was characterized by the presence of manganite/hausmannite core-shell nanowires. Hem and Lind (1983) documented that the hausmannite nanocrystals precipitated on manganite wires at intermediate stages of Mn(II) oxidation toward the final Mn(IV)-bearing oxide (i.e. pyrolusite, MnO_2) in an open system with respect to O_2 gas. They considered that the formation of hausmannite was attributed to the cyclic processes of oxidation and disproportionation reactions. According to TEM images presented by Hem and Lind (1983), their pseudocubic hausmannite nanocrystals appear to be physically attached on the manganite needles. This morphology is quite different from the core-shell structure observed in the present study (Figs. 8 and 9). The formation of manganite is thermodynamically more favorable than that of hausmannite when decreasing the concentration of aqueous Mn (II) at pH 7.5 (Fig. 15). This suggests that the formation mechanism of the core-shell nanowire would be different from the aforementioned cyclic oxidation and disproportionation process as proposed by Hem and Lind (1983).

Corrosive replacement of manganite by hausmannite is another possible mechanism of the core-shell nanowire formation. It can be described as the reductive transformation of manganite under O_2 depleted conditions:

$$2\gamma\text{–}MnOOH_c + {Mn^{2+}}_{aq} \rightarrow Mn_3O_{4c} + 2H^+. \quad (4)$$

The thermodynamic equilibrium curve of reaction (4) is also illustrated in Fig. 15. As the system becomes depleted in Mn(II), the formation of hausmannite becomes unfavorable. Moreover, if the reductive transformation of reaction (4) is the case, the core-shell structure must be a snapshot of replacement processes by hausmannite which proceeds toward the core of precursor manganite nanowire. Such corrosive replacement is expected to proceed so as to maintain similar dimensions to the original nanowire. In our experimental observation, however, the third stage nanowires became longer and wider than the second stage nanowires as the reaction proceeded (Fig. 6). The sharp interface between hausmannite outer-shell and manganite core (Fig. 9b) is unlikely to be achieved by inward replacement (Putnis, 2009). Rather, the hausmannite outer-shell appears to be in coherent contact with the surface of the core manganite. These morphological features suggest that the core-shell structure is not the product of corrosive replacement by hausmannite after the precursor manganite nanowire.

Based on the FFT pattern analyses, the interface shown in Fig. 9b is designated as the interphase interface between manganite [1 2 $\bar{1}$] and hausmannite [0 1 $\bar{2}$]. A multislice image simulation of the proposed interface has been performed by assuming that the manganite (101) plane runs parallel to hausmannite (2 0 0), and the two crystals are separated by manganite (1 1 $\bar{1}$) plane (inset of Fig. 9b). The intersecting angle between (1 1 $\bar{1}$) lattice fringes of manganite and (2 0 0) lattice fringes of hausmannite coincides well with the obtained HRTEM image. Although it is difficult to confirm how two phases are terminated from the obtained HRTEM image and to compare it with the simulated image, the results of simulation indicate that the proposed interface is likely coherent. Taking the structural coherency into account, the formation of hausmannite outer-shell appears to be catalyzed by the core manganite nanowire itself. Unfortunately, the semiconducting properties of manganite are not available. The surfaces of manganite nanowires are likely to be negatively charged at pH

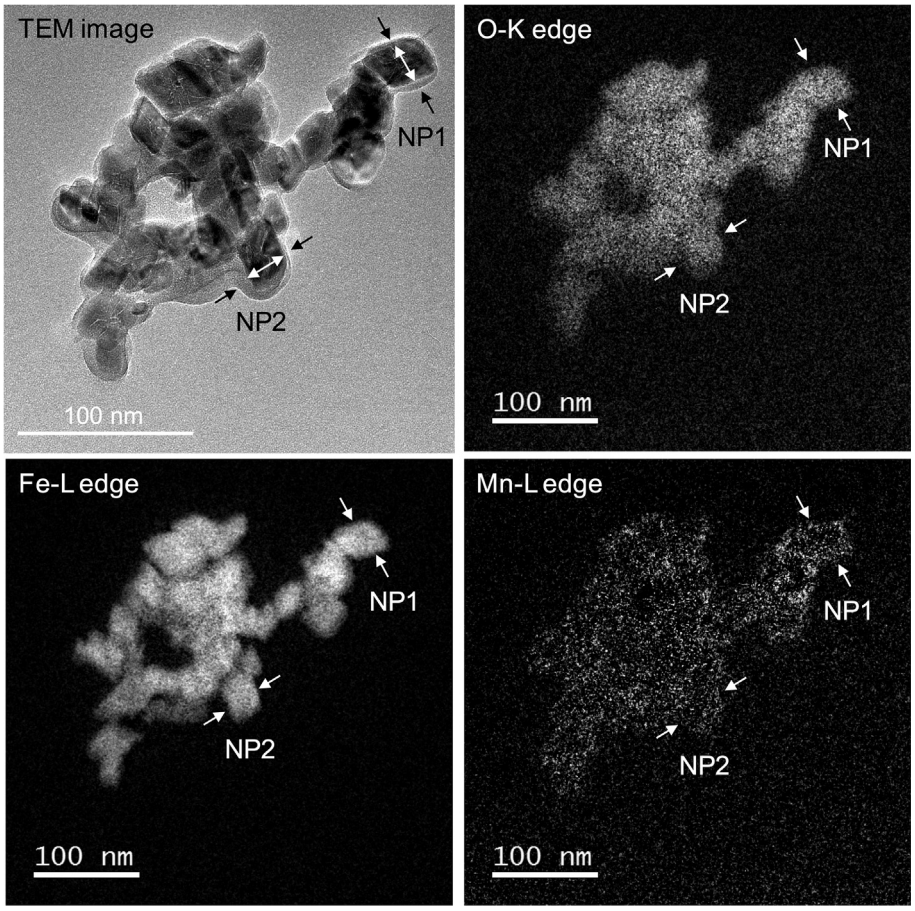

Fig. 13. EFTEM O, Fe and Mn maps and the corresponding BF image of hematite NPs. The diameters of NP1 and NP2 measured on the TEM image and elemental maps are summarized in Table 1. The double-headed arrows and single head arrows in the TEM image show the "inner" and "outer" diameters, respectively.

Table 1
The diameters of post-reaction hematite NPs measured on the TEM image and EFTEM elemental maps in Fig. 13.

		NP1	NP2
Diameter on TEM image (nm)	Outer	33.4	39.1
	Inner	25.7	22.3
Diameter on EFTEM map (nm)	O-K map	32.5	37.9
	Fe-L map	28.6	27.9
	Mn-L map	32.3	37.9

7.5, inferred from the point of zero charge (Shaughnessy et al., 2003). The negatively charged faces facilitate adsorption of aqueous Mn(II) ions remaining in the suspension. Once Mn(II) is adsorbed on the surface, the manganite would accept electrons from adsorbed Mn(II) and oxidize it to form hausmannite, depending on the relative positions of E_{CB} and E_F against the redox potential of hausmannite/Mn^{2+} redox couple. Hausmannite is known as a p-type semiconductor with holes as major carriers. If manganite has n-type semiconducting properties (Weaver et al., 2002), the ET from manganite to newly formed hausmannite would further accelerate the oxidation of adsorbed Mn(II) by so-called p-n junction mechanism. Conclusively, the observed structural features of core-shell nanowires are possibly linked to an autocatalytic reaction related to the semiconducting nature of manganite. Further studies on the electrochemical ability of manganite nanowires would help to determine the conversion mechanism.

4.5. Geochemical implications

The nanoscale direct observations of reaction products have shown that the Mn oxides formed by the Mn(II) oxidation in the presence of nanohematite surfaces are the product of complex mechanisms relating to the ET between Mn(II) and hematite, sequential crystallization and phase transformation from metastable phases to stable phase, and autocatalytic reactions between the product Mn oxides themselves and $Mn(II)_{aq}$. Although further clarification of each process is desired, this study has emphasized the importance of characterizing structural, chemical and morphological changes of solid phase products to understand the redox chemistry in the system. Besides the formation mechanisms of Mn oxide nanowires, the geochemical importance of finding manganite/hausmannite core-shell nanowires should be emphasized. This particular occurrence has never been observed in laboratory experiments

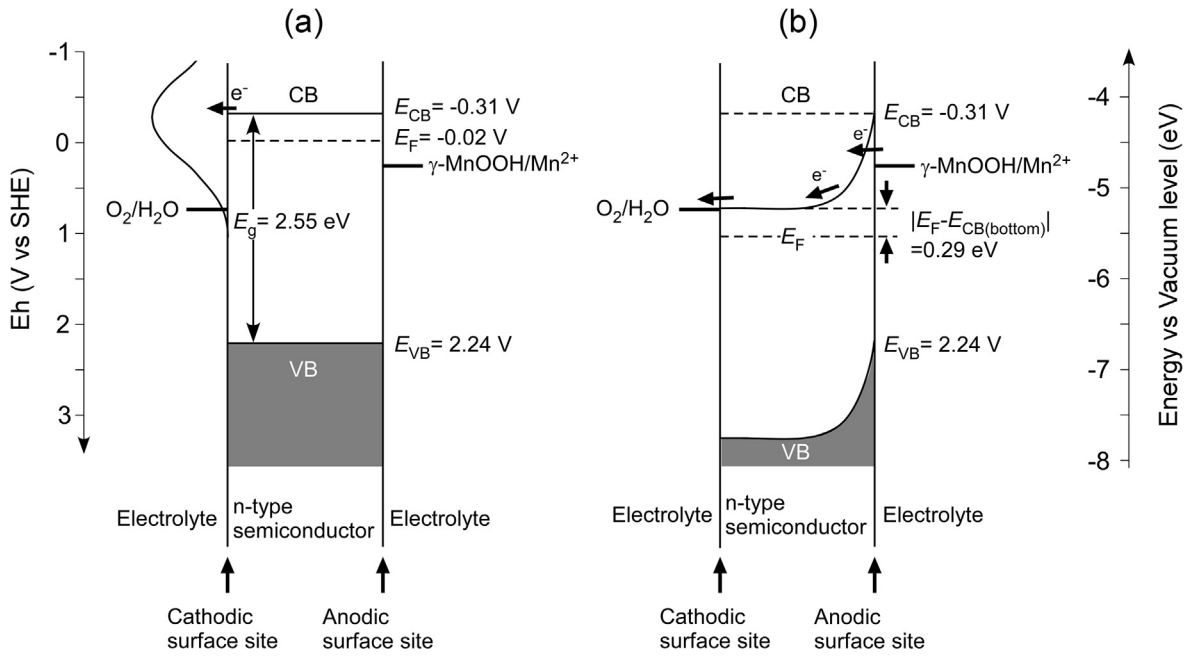

Fig. 14. Schematic diagram of the interfacial energetics of a hematite NP at pH 7.5. (a) The positions of the conduction band edge, Fermi level and valence band edge at the flat band condition. The Gaussian curve on the left depicts distributions of empty electron levels of dissolved O_2 with a typical reorganization energy of 1 eV (Finklea, 2007). The O_2 adsorbed on the cathodic surface site is reduced by capturing free electrons in the n-type semiconductor hematite. (b) The interfacial energetics when band bending is induced by the ET from hematite to adsorbed O_2. CB: conduction band, VB: valence band; E_g: band gap, E_F: Fermi level, E_{CB}: conduction band energy at the flat band condition, E_{VB}: valence band energy at the flat band condition, $|E_F - E_{CB(bottom)}|$: the energy gap between E_F and the bottom of the conduction band.

until now. Further, this nanomaterial has never been observed in the field, although Hochella et al. (1999) reported the occurrence of hydrohetaerolite (a polymorph of hausmannite, and a Zn, Mn oxide-hydrate mineral) in the form of 5–10 nm wide nanowires growing in association with the mineral ferrihydrite (a hydrous ferric oxyhydroxide nanomineral). This nanowire occurrence was in a mine drainage floodplain setting where hydrohetaerolite growth helped immobilize toxic levels of Zn in a highly contaminated area.

The occurrence of mineral nanowires may be much more common in nature than we presently realize. The discovery of bacterial nanowires is a good example of demonstrating how easily scientists can miss important natural nanomaterials without appropriate sample preparation and/or analytical techniques. The bacterial nanowire, an organic filament-like electrically conductive appendage produced by metal-reducing bacteria, had not been found/recognized until recently because specimens need a specific preparation that was not a routine method (Reguera et al., 2005; Gorby et al., 2006). However, once these nanowires were recognized, they have been increasingly found in various types of microbes, and are now recognized as a key mechanism that transfers electrons from bacteria to minerals (e.g. Shi et al., 2016). Concerning minerals, morphologies described as acicular, capillary, fibrous, filiform, or wiry all connote mangannite-like morphologies. Although such morphologies are not exactly extensively common in the mineral world, they are not uncommon either. As sample preparation and TEM characterization of intact sediment, soil, and wetland samples become more common and routine, it is likely that more nanominerals and mineral nanoparticles with nanowire morphologies will be described.

Nanominerals and mineral nanoparticles with different shapes can lead to the formation of preferred reaction sites due to their shape or surface anisotropy. Navrotsky (2011) exemplified ZnO nanorods as having a higher surface energy than ZnO nanoparticles. Even though the shape effects of nanomaterials are acknowledged, how shape of nanoscale minerals influences the efficiency of reactions with the surrounding environment has not been thoroughly explored. This situation is partly because shape is difficult or effectively impossible to garner using high through-put analytical techniques such as solution analysis or powder XRD. High resolution SEM, TEM, and atomic force microscopy (AFM) imaging remain the best tools for gaining precise size and shape information.

Core-shell structured nanomaterials also seem to be rare in nature, but again, simply because it is difficult to observe, it may be, in reality, very common, or at least not rare. Moreover, as such nanoscale structural heterogeneity will be most practically and reliably observed by advanced TEM techniques, they are likely to be found much more frequently than presently assumed in nature. In our study, the formation of the hausmannite outer-shell completely changes what the solution sees; the manganite–$Mn(II)_{aq}$ interactions becomes hausmannite–$Mn(II)_{aq}$ interactions. The nanoscale characterizations by HRTEM and analytical TEM became crucial to construct a complete picture of the reactions between this nanoscale mineral and its surround-

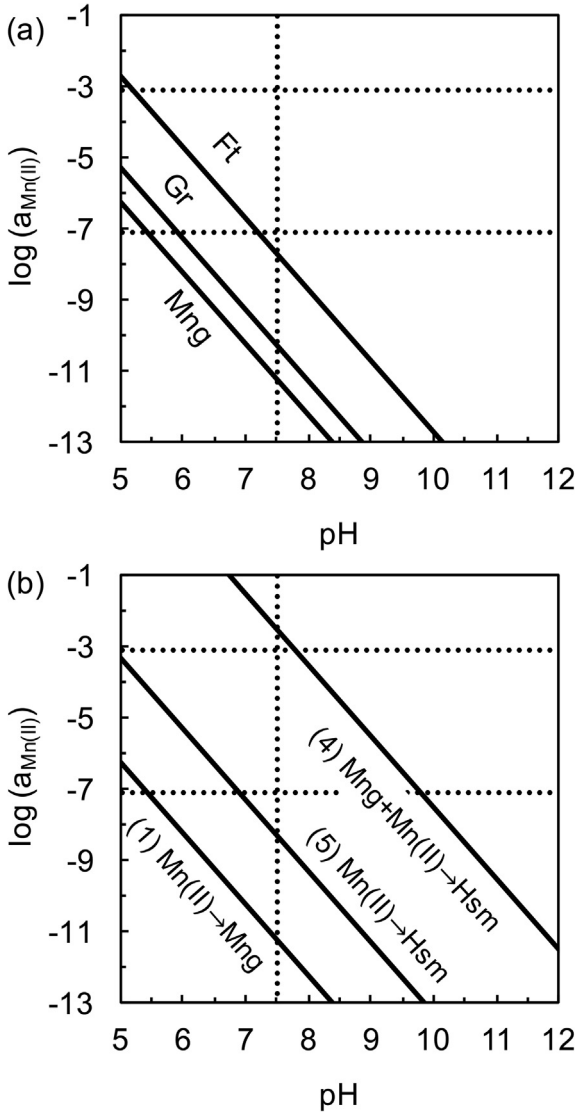

Fig. 15. (a) Theoretical log($a_{Mn(II)}$) versus pH stability lines of reaction (1) with different MnOOH polymorphs. (b) Stability lines for reaction (1) with manganite, reaction (4) with hausmannite, and also with Mn(II) oxidation into hausmannite expressed in reaction (5) as $Mn^{2+}_{aq}+\frac{1}{6}O_{2aq}+H_2O \rightarrow \frac{1}{3}Mn_3O_4+2H^+\#$ (5). The conditions at the beginning of reaction ($[Mn^{2+}]=10^{-3}$ M, pH 7.5) and after 48 h of reaction ($[Mn^{2+}]=10^{-7}$ M, pH 7.5), estimated from Veeramani et al. (2013), are also shown in the figure. Thermodynamic data are cited from Bard et al. (1985) and Bricker (1965). The activity coefficient of Mn^{2+} is 0.87 (Stumm and Morgan 1996). The calculation was done assuming $[O_{2aq}]=10^{-3.55}$ M at total pressure of 1 atm and 25 °C. Gr: groutite, Ft: feitknechtite, Mng: manganite, Hsm: hausmannite.

ing environment. Although these two minerals were not used in an extensive experimental aqueous Pb sorption efficiency study of a number of Mn-oxides (O'Reilly and Hochella, 2003), it was clear from this study that Pb sorption efficiencies vary dramatically depending on the Mn-oxide species, and its size, shape, exact composition, and so on.

This study shows that the structure of Mn oxide nanowires changes continuously as a result of both nanohematite- and self-catalyzed Mn(II) oxidation. The formation of a 2–3 nm thick hausmannite outer-shell on the manganite nanowires observed in this study will change the redox chemistry and phase stability in the system suggesting that the self-catalytic reactions are as important as the nanohematite-catalyzed reactions. Characterization of nanoscale interfacial changes in structure and chemistry of nanoscale minerals will help in the understanding of kinetic and thermodynamic phenomena in natural environments.

ACKNOWLEDGMENTS

This material is based upon work supported by the National Science Foundation (NSF) and the Environmental Protection Agency (EPA) under NSF Cooperative Agreement EF-0830093 and DBI-1266252, Center for the Environmental Implications of NanoTechnology (CEINT). Any opinions, findings, conclusions, or recommendations expressed in this material are those of the author(s) and do not necessarily reflect the views of the NSF or the EPA. This work has not been subjected to EPA review and no official endorsement should be inferred. Funding for this project was partly provided by DOE BES Geosciences (DE-FG02-06ER15786) and facilities were made available through Virginia Tech's Institute for Critical Technology and Applied Science Nanoscale Characterization and Fabrication Laboratory (ICTAS-NCFL).The authors also used shared facilities at the Virginia Tech National Center for Earth and Environmental Nanotechnology Infrastructure (NanoEarth), a member of the National Nanotechnology Coordinated Infrastructure (NNCI), supported by NSF (ECCS 1542100). The authors are grateful to Dr. F. Marc Michel for supporting XRD analyses. We also thank Dr. Deborah Aruguete at PennState Behrend and Dr. Harish Veeramani at Carleton University for assistance with the initial experiment setup.

REFERENCES

Ahn C. C. (2004) *Transmission Electron Energy Loss Spectrometry in Materials Science and the EELS Atlas*. Wiley-VCH, New York.

Aminoff G. (1926) Über die Kristallstruktur von Hausmannit ($MnMn_2O_4$). *Z. Kristallogr.* **64**, 475–490.

Banfield, J. F. and Zhang, H. (2001) Nanoparticles in the environment. In Rev. Mineral. Geochem (Eds. J. F. Banfield, A. Navrotsky), pp. 1–58.

Baes, C.F. and Mesmer, R. S. The Hydrolysis of Cations, 1976, John Wiley and Sons, Inc.; New York.

Bard A. J., Parsons R. and Jordan J. (1985) *Standard Potentials in Aqueous Solution*. Marcel Dekker Inc, New York.

Bodeï S., Manceau A., Geoffroy N., Baronnet A. and Buatier M. (2007) Formation of todorokite from vernadite in Ni-rich hemipelagic sediments. *Geochim. Cosmochim. Acta* **71**, 5698–5716.

Bricker O. (1965) Some stability relations in the system Mn-O_2-H_2O at 25 °C and one atmosphere total pressure. *Am. Mineral.* **50**, 1296–1354.

Chernyshova I. V., Ponnurangam S. and Somasundaran P. (2010) On the origin of an unusual dependence of (bio)chemical reactivity of ferric hydroxides on nanoparticle size. *Phys. Chem. Chem. Phys.* **12**, 14045–14056.

Chernyshova I. V., Ponnurangam S. and Somasundaran P. (2011a) Effect of nanosize on catalytic properties of ferric (hydr)oxides in water: Mechanistic insights. *J. Catal.* **282**, 25–34.

Chernyshova I. V., Ponnurangam S. and Somasundaran P. (2011b) Tailoring (bio)chemical activity of semiconducting nanoparticles: critical role of deposition and aggregation. *J. Am. Chem. Soc.* **133**, 9536–9544.

Cornell, R. M. and Schwertmann, U. (2003) The Iron Oxides: Structures, Properties, Reactions, Occurrences and Uses. Second ed. Wiley-VCH, Weinheim.

Davies S. H. R. and Morgan J. J. (1989) Manganese(II) oxidation kinetics on metal oxide surfaces. *J. Colloid Interface Sci.* **129**, 63–77.

Diem D. and Stumm W. (1984) Is dissolved Mn^{2+} being oxidized by O_2 in absence of Mn-bacteria or surface catalysts?. *Geochim. Cosmochim. Acta* **48** 1571–1573.

Egerton R. F. (2011) *Electron Energy-Loss Spectroscopy in the Electron Microscope*. Springer, New York.

Finklea, H. O. (2007) Electron transfer. In Encyclopedia of Electrochemistry (eds. M. Fujihira, I. Rubinstein, J.F. Rusling), Wiley-VCH Verlag GmbH&Co., Weinheim, pp. 623–650.

Frierdich A. J., Spicuzza M. J. and Scherer M. M. (2016) Oxygen isotope evidence for Mn(II)-catalyzed recrystallization of manganite (γ-MnOOH). *Environ. Sci. Technol.* **50**, 6374–6380.

Fritsch S., Post J. E. and Navrotsky A. (1997) Energetics of low-temperature polymorphs of manganese dioxide and oxyhydroxide. *Geochim. Cosmochim. Acta* **61**, 2613–2616.

Gardner R. F. G., Sweett F. and Tanner D. W. (1963) The electrical properties of alpha ferric oxide—II Ferric oxide of high purity. *J. Phys. Chem. Solids* **24**, 1183–1196.

Gorby Y. A., Yanina S., McLean J. S., Rosso K. M., Moyles D., Dohnalkova A., Beveridge T. J., Chang I. S., Kim B. H., Kim K. S., Culley D. E., Reed S. B., Romine M. F., Saffarini D. A., Hill E. A., Shi L., Elias D. A., Kennedy D. W., Pinchuk G., Watanabe K., Ishii S. i., Logan B., Nealson K. H. and Fredrickson J. K. (2006) Electrically conductive bacterial nanowires produced by Shewanella oneidensis strain MR-1 and other microorganisms. *Proc. Natl. Acad. Sci.* **103**, 11358.

Grangeon S., Manceau A., Guilhermet J., Gaillot A.-C., Lanson M. and Lanson B. (2012) Zn sorption modifies dynamically the layer and interlayer structure of vernadite. *Geochim. Cosmochim. Acta* **85**, 302–313.

Hem J. D. and Lind C. J. (1983) Nonequilibrium models for predicting forms of precipitated manganese oxides. *Geochim. Cosmochim. Acta* **47**, 2037–2046.

Hochella M. F., Kasama T., Putnis A., Putnis C. V. and Moore J. N. (2005a) Environmentally important, poorly crystalline Fe/Mn hydrous oxides: Ferrihydrite and a possibly new vernadite-like mineral from the Clark Fork River Superfund Complex. *Am. Mineral.* **90**, 718–724.

Hochella M. F., Moore J. N., Golla U. and Putnis A. (1999) A TEM study of samples from acid mine drainage systems: metal-mineral association with implications for transport. *Geochim. Cosmochim. Acta* **63**, 3395–3406.

Hochella M. F., Moore J. N., Putnis C. V., Putnis A., Kasama T. and Eberl D. D. (2005b) Direct observation of heavy metal-mineral association from the Clark Fork River Superfund Complex: implications for metal transport and bioavailability. *Geochim. Cosmochim. Acta* **69**, 1651–1663.

Jambor J. L. and Dutrizac J. E. (1998) Occurrence and constitution of natural and synthetic ferrihydrite, a widespread iron oxyhydroxide. *Chem. Rev. (Washington, DC, U. S.)* **98**, 2549–2586.

Junta J. and Hochella M. F. (1994) Manganese(II) oxidation at mineral surfaces – a microscopic and spectroscopic study. *Geochim. Cosmochim. Acta* **58**, 4985–4999.

Kennedy J. H. and Frese K. W. (1978) Flatband potentials and donor densities of polycrystalline α -Fe_2O_3 determined from Mott-Schottky plots. *J. Electrochem. Soc.* **125**, 723–726.

Kirillov S. A., Aleksandrova V. S., Lisnycha T. V., Dzanashvili D. I., Khainakov S. A., García J. R., Visloguzova N. M. and Pendelyuk O. I. (2009) Oxidation of synthetic hausmannite (Mn_3O_4) to manganite (MnOOH). *J. Mol. Struct.* **928**, 89–94.

Kohler T., Armbruster T. and Libowitzky E. (1997) Hydrogen bonding and Jahn-Teller distortion in groutite, α-MnOOH, and manganite, γ-MnOOH, and their relations to the manganese dioxides ramsdellite and pyrolusite. *J. Solid State Chem.* **133**, 486–500.

Kurata H. and Colliex C. (1993) Electron-energy-loss core-edge structures in manganese oxides. *Physical Review B* **48**, 2102–2108.

Lan S., Wang X., Xiang Q., Yin H., Tan W., Qiu G., Liu F., Zhang J. and Feng X. (2017) Mechanisms of Mn(II) catalytic oxidation on ferrihydrite surfaces and the formation of manganese (oxyhydr)oxides. *Geochim. Cosmochim. Acta* **211**, 79–96.

Leapman R. D. and Swyt C. R. (1988) Separation of overlapping core edges in electron energy loss spectra by multiple-least-squares fitting. *Ultramicroscopy* **26**, 393–403.

Lefkowitz J. P., Rouff A. A. and Elzinga E. J. (2013) Influence of pH on the reductive transformation of birnessite by aqueous Mn(II). *Environ. Sci. Technol.* **47**, 10364–10371.

Luther G. W. (2016) *Inorganic Chemistry for Geochemistry and Environmental Sciences*. John Wiley & Sons Ltd., Chinchester.

Madden A. S. and Hochella M. F. (2005) A test of geochemical reactivity as a function of mineral size: manganese oxidation promoted by hematite nanoparticles. *Geochim. Cosmochim. Acta* **69**, 389–398.

Maigné A. and Twesten R. D. (2009) Review of recent advances in spectrum imaging and its extension to reciprocal space. *J. Electron Microsc.* **58**, 99–109.

Markov I. V. (1995) *Crystal Growth for Beginners*. World Scientific, Singapore.

McAlpine N. S. and Fredlein R. A. (1983) Oxygen reduction on titanium-doped α-Fe_2O_3 electrodes in aqueous alkali. *Aust. J. Chem.* **36**, 11–17.

Momma K. and Izumi F. (2011) VESTA 3 for three-dimensional visualization of crystal, volumetric and morphology data. *J. Appl. Crystallogr.* **44**, 1272–1276.

Morrison S. R. (1990) *The Chemical Physics of Surfaces*, second ed. Plenum, New York.

Murray J. W., Dillard J. G., Giovanoli R., Moers H. and Stumm W. (1985) Oxidation of Mn(II): initial mineralogy, oxidation state and ageing. *Geochim. Cosmochim. Acta* **49**, 463–470.

Navrotsky, A., 2001. Thermochemistry of nanomaterials. In Nanoparticles in Environment (Eds. Banfield, J.F., Navrotsky, A.). Mineralogical Society of America, Washington D.C., pp. 73–103.

Navrotsky A. (2011) Nanoscale effects on thermodynamics and phase equilibria in oxide systems. *ChemPhysChem* **12**, 2207–2215.

Navrotsky A., Ma C., Lilova K. and Birkner N. (2010) Nanophase transition metal oxides show large thermodynamically driven shifts in oxidation-reduction equilibria. *Science* **330**, 199.

O'Reilly S. E. and Hochella M. F. (2003) Lead sorption efficiencies of natural and synthetic Mn and Fe-oxides. *Geochim. Cosmochim. Acta* **67**, 4471–4487.

Paterson J. H. and Krivanek O. L. (1990) ELNES of 3d transition-metal oxides: II. Variations with oxidation state and crystal structure. *Ultramicroscopy* **32**, 319–325.

Post J. E. (1999) Manganese oxide minerals: crystal structures and economic and environmental significance. *Proc. Natl. Acad. Sci.* **96**, 3447–3454.

Putnis, A. (2009) Mineral replacement reactions. In Thermodynamics and Kinetics of Water-Rock Interaction. (Eds. Oelkers, E.H., Schott, J.), Mineralogical Society of America and Geochemical Society, Chantilly, pp. 87–124.

Rask J. H., Miner B. A. and Buseck P. R. (1987) Determination of manganese oxidation states in solids by electron energy-loss spectroscopy. *Ultramicroscopy* **21**, 321–326.

Reguera G., McCarthy K. D., Mehta T., Nicoll J. S., Tuominen M. T. and Lovley D. R. (2005) Extracellular electron transfer via microbial nanowires. *Nature* **435**, 1098.

Schwertmann U. and Cornell R. M. (2000) *Iron Oxides in the Laboratory: Preparation and Characterization*. Wiley-VCH, Weinheim, Germany.

Schoonen M. A. and Strongin D. R. (2005) Catalysis of electron transfer reactions at mineral surfaces. In *Environmental Catalysis* (ed. V. Grassian). CRC Press, Boca Raton, pp. 37–60.

Shaughnessy D. A., Nitsche H., Booth C. H., Shuh D. K., Waychunas G. A., Wilson R. E., Gill H., Cantrell K. J. and Serne R. J. (2003) Molecular interfacial reactions between Pu (VI) and manganese oxide minerals manganite and hausmannite. *Environ. Sci. Technol.* **37**, 3367–3374.

Shi L., Dong H., Reguera G., Beyenal H., Lu A., Liu J., Yu H.-Q. and Fredrickson J. K. (2016) Extracellular electron transfer mechanisms between microorganisms and minerals. *Nat. Rev. Microbiol.* **14**, 651.

Stumm W. and Giovanoli R. (1976) On the nature of particulate manganese in simulated lake waters. *Chimia* **30**, 423–425.

Stumm W. and Morgan J. J. (1996) *Aquatic Chemistry: Chemical Equilibria and Rates in Natural Waters*. Wiley, New York.

Sung W. and Morgan J. J. (1981) Oxidative removal of Mn(II) from solution catalysed by the γ-FeOOH (lepidocrocite) surface. *Geochim. Cosmochim. Acta* **45**, 2377–2383.

Tan H., Verbeeck J., Abakumov A. and Van Tendeloo G. (2012) Oxidation state and chemical shift investigation in transition metal oxides by EELS. *Ultramicroscopy* **116**, 24–33.

Tebo B. M., Bargar J. R., Clement B. G., Dick G. J., Murray K. J., Parker D., Verity R. and Webb S. M. (2004) Biogenic manganese oxides: Properties and mechanisms of formation. *Annu. Rev. Earth Planet. Sci.* **32**, 287–328.

Veeramani H., Aruguete D., Monsegue N., Murayama M., Dippon U., Kappler A. and Hochella M. F. (2013) Low-temperature green synthesis of multivalent manganese oxide nanowires. *ACS Sustain Chem Eng* **1**, 1070–1074.

Villalobos M., Bargar J. and Sposito G. (2005a) Mechanisms of Pb (II) sorption on a biogenic manganese oxide. *Environ. Sci. Technol.* **39**, 569–576.

Villalobos M., Bargar J. and Sposito G. (2005b) Trace metal retention on biogenic manganese oxide nanoparticles. *Elements* **1**, 223–226.

Wang G., Ling Y., Wheeler D. A., George K. E. N., Horsley K., Heske C., Zhang J. Z. and Li Y. (2011) Facile synthesis of highly photoactive α-Fe_2O_3-based films for water oxidation. *Nano Lett.* **11**, 3503–3509.

Wang X., Zhu M., Lan S., Ginder-Vogel M., Liu F. and Feng X. (2015) Formation and secondary mineralization of ferrihydrite in the presence of silicate and Mn(II). *Chem. Geol.* **415**, 37–46.

Weaver R. M., Hochella M. F. and Ilton E. S. (2002) Dynamic processes occurring at the Cr^{III}_{aq}-manganite (γ-MnOOH) interface: simultaneous adsorption, microprecipitation, oxidation/reduction, and dissolution. *Geochim. Cosmochim. Acta* **66**, 4119–4132.

Xu Y. and Schoonen M. A. A. (2000) The absolute energy positions of conduction and valence bands of selected semiconducting minerals. *Am. Mineral.* **85**, 543–556.

Associate editor: Owen Duckworth